Research Square

Preprints are preliminary reports that have not undergone peer review.
They should not be considered conclusive, used to inform clinical practice,
or referenced by the media as validated information.

Understanding and Suppressing Gas Evolution in Lithium Metal Batteries with Ether-Based Electrolytes

Hansen Wang

wanghansen0830@gmail.com

Contemporary Amperex Technology Co., Limited (CATL) https://orcid.org/0000-0002-6738-1659

Yuchun Wang

Contemporary Amperex Technology Co., Limited (CATL)

Samantha Kung

Contemporary Amperex Technology Co., Limited (CATL)

Ziman Cai

Contemporary Amperex Technology Co., Limited (CATL)

Juanjuan Sun

Contemporary Amperex Technology Co., Limited (CATL)

Haoran Li

Contemporary Amperex Technology Co., Limited (CATL)

Jinding Liang

Contemporary Amperex Technology Co., Limited (CATL)

Lu Bai

Contemporary Amperex Technology Co., Limited (CATL)

Erxiao Wu

Contemporary Amperex Technology Co., Limited (CATL)

Ulderico Ulissi

Contemporary Amperex Technology Co., Limited (CATL)

Xiaolin Yan

Contemporary Amperex Technology Co., Limited (CATL)

Xiaonan Luo

Contemporary Amperex Technology Co., Limited (CATL)

Na Liu

Contemporary Amperex Technology Co., Limited (CATL)

Chuying Ouyang

Contemporary Amperex Technology Co., Limited (CATL)

Article

Keywords:

Posted Date: February 27th, 2025

DOI: https://doi.org/10.21203/rs.3.rs-6034057/v1

License: This work is licensed under a Creative Commons Attribution 4.0 International License.
Read Full License

Additional Declarations: Yes there is potential Competing Interest. All authors are employed by Contemporary Amperex Technology Co., Limited (CATL).

Version of Record: A version of this preprint was published at Nature Chemistry on August 20th, 2026. See the published version at https://doi.org/10.1038/s41557-026-02219-1.

Abstract

Understanding and suppressing gas evolution in lithium secondary batteries are critical to optimizing battery performance and ensuring safe operation.[1,2] However, no systematic investigations of gas evolution in ether-based lithium metal batteries (LMBs) have been conducted despite the enticing prospects of LMBs for achieving ultrahigh energy density.[3–5] In this work, gas generation in ether electrolyte-based LMBs was quantified and the underlying redox mechanisms were elucidated. Through studying cathode and anode half-cells, it was determined that CO_2 and CO gas were generated at the cathode and CH_4 gas at the anode. Notably, CO_2 and CO were not observed in the full cell as they were consumed at the anode, reacting with lithium to produce solid Li compounds such as Li_2CO_3. CH_4 generated at the anode is the major contributor of gas generated in the full cell, though its evolution during cycling is not immediate and occurs after an onset point. The total gas volume generated increases dramatically with increasing temperature and decreasing electrolyte concentration. Based on these findings, electrolyte engineering and anode surface activation strategies were explored to control CH_4 production and hence overall gas evolution. In particular, the anode activation approach resulted in increased Li nucleation sites and improved Li deposition morphology, leading to significantly suppressed interfacial reactions, thus delaying the onset of gas evolution by 800% and increasing the cycling life by 400%. Achieving these improvements without altering the electrolyte formulation demonstrates the potential broad applicability of anode activation across various electrolyte chemistries. The performance enhancements beyond merely suppressing gas generation advances the prospects of safer and higher-performing LMBs.

Introduction

Lithium (Li) metal anodes, due to their high specific capacity of 3860 mAh/g,[3–5] are ideal for the development of high energy battery systems that could enable electric aviation, such as electric vertical take-off and landing (eVTOL) aircraft, and long-range electric vehicles.[5–8] Therefore, enhancing the cycling performance of lithium metal batteries (LMBs) has been a subject of constant interest and research.[9–17] However, gas evolution during LMB operation remains poorly understood, especially for recently developed ether-based electrolytes, which are more compatible with Li metal than conventional electrolytes due to their intrinsic cathodic stability.[1,2,9,18–22] Uncontrolled gas evolution can rupture pouch cells and cause unwanted venting in prismatic and cylindrical cells, leading to serious safety risks such as electrolyte leakage and the release of toxic and flammable gases. Operation at elevated temperatures could further exacerbate gas evolution and the accompanying hazards.[2,23] In particular, during the high-rate operations of eVTOLs, cell temperatures above 50°C can develop.[24,25] Simulations of high energy lithium-ion CATL prismatic cells indicate that temperatures increase with the discharging rate, reaching 42°C at 4 C discharge and 62°C at 8 C (Supplementary Information, Fig. S1). This temperature increase is expected to be aggravated at the pack level in eVTOLs due to more limited heat dissipation and the minimal thermal management necessitated by weight constraints.[26,27] Therefore, it

is critical to understand and suppress gas evolution in LMBs at elevated temperatures (e.g., 45–70°C) to ensure safe operation under practical working conditions.

Here, we present the first study to quantify gas evolution under operando conditions and elucidate its mechanism in LMBs with high concentration ether-based electrolytes (HCE) and lithium nickel manganese cobalt oxide (NMC811) cathodes. After cycling at 45–70°C, the dominant gas component observed was methane (CH_4) gas generated at the anode. Moderate amounts of carbon monoxide (CO) and carbon dioxide (CO_2) gas were generated at the cathode and solidified through cross-talk reactions with the anode and thus not detected in the full cell.

Minimal gas was detected during initial cycling of the full cell and gas evolution dominated by CH_4 generation only began after a variable number of cycles. The onset of gas evolution shifted forward in time both when increasing the cycling temperature and decreasing the electrolyte concentration. The underlying gas generation pathways at the electrode-electrolyte interfaces were analyzed using first-principles simulations. Experimental and computational results suggest that the onset of CH_4 evolution is linked to the accumulation of the methyllithium ($LiCH_3$) precursor, a decomposition intermediate of the 1,2-dimethoxyethane (DME) solvent.

According to the experimental results, preventing CH_4 generation following DME decomposition is key to addressing gas evolution in DME-based LMBs. A localized high concentration electrolyte (LHCE) and a fluorinated-ether electrolyte (FEE) were tested as alternative ether electrolytes, as they are unlikely to support CH_4 formation. While these formulations successfully suppressed gas evolution, they also significantly reduced rate performance, which is detrimental for high-power applications in electric aviation. To overcome this, we propose a novel approach to activate the lithium anode by pre-stripping the surface to form sites conducive to more homogeneous Li deposition. This approach resulted in remarkable suppression of the CH_4-forming interfacial chemical reactions with minimal impact on the rate performance. The onset of gas generation was delayed by almost 800% and the cycle life was increased by over 400%. Additionally, consumption of the Li salt and DME through interfacial reactions was reduced by 82.61% and 82.46%, respectively.

By providing a comprehensive mechanistic understanding of and viable solutions for suppressing gas evolution in ether-based LMBs, this work paves the way for LMB commercialization, offering long cycle life, high energy density, and exceptional safety characteristics.

Overview of Gas Evolution in LMB

Gas evolution was investigated for the Li||NMC single layer stack (SLS) pouch cell shown schematically in Fig. 1a. The electrolyte used was 4 M lithium bis(fluorosulfonyl)imide (LiFSI) in DME. Figure 1b shows the voltage versus time plot of the Li||NMC full cell cycled at 60 ℃ between 2.8 and 4.3 V with 0.2 C charge and 0.5 C discharge rates. Cell volume changes (ΔVolume in Fig. 1b) were tracked by an

Archimedes *in situ* gas analyzer.[28] Following a small initial volume increase and a gradual volume decline (between ~ 500–3000 min), an abrupt and dramatic volume increase was observed after an onset point of 5 cycles (~ 3000 min). After 28 cycles, ~ 9 mL gas was produced, accompanied by significant swelling of the cell (Fig. S2). The volume increase occurred on top of minor oscillations that track the reversible cell volume changes during charging and discharging, matching the changes in the voltage.

Systematic investigation of the full cell was supported by studies of the anode and cathode half-cells, which independently revealed the gas evolution characteristics at each electrode. In this study, anode and cathode half-cells are defined as Li||lithiated LFP (Li||LFP) and delithiated LFP||NMC cells (d-LFP||NMC) (Fig. 1a, "half-cell test systems"), respectively. The lithium iron phosphate (LFP, $LiFePO_4$) counter electrodes (Fig. 1a, "inert electrodes") are designated as "inert" in the context of this study since they do not generate gas when cycled from an SOC of 0 to 100% at 60 ℃ for over 30 cycles (Fig. S3c). Shown in Fig. 1c are the normalized volume fractions of gases generated in the full cell, anode half-cell, and cathode half-cell. The total volumes were obtained from *ex situ* measurements and the proportions of the constituent gas components were determined from gas chromatography (GC) results. The total volumes were normalized by the design capacity and cycling time (see Methods) to facilitate comparison. The results for the anode half-cell closely aligned with that of the full cell, with both producing a normalized gas volume of ~ 0.3 mL/Ahžh and consisting of methane (CH_4) as the dominant (~ 97%) component (Tables S2 and S5). Trace components include ethane (C_2H_6), ethylene (C_2H_4), acetylene (C_2H_2), propylene (C_3H_6), propane (C_3H_8), hydrogen (H_2), and oxygen (O_2). In contrast, the normalized gas volume for the cathode half-cell was ~ 0.1 mL/Ahžh, dominated by carbon monoxide (CO, ~ 43%) and carbon dioxide (CO_2, ~ 56%) (Table S3), both of which were absent in the full cell.

A cross-talk phenomenon (Fig. 1d) was proposed to account for the discrepancy in CO and CO_2 content. When CO and CO_2 produced at the NMC cathode were deposited as lithium compounds such as lithium carbonate (Li_2CO_3)[29–31] at the Li anode in the Li||NMC full cell, the two gases could not be detected. The resulting Li_2CO_3 cross-talk product in particular could be readily detected using titration-mass spectroscopy (T-MS),[32,33] with sulfuric acid (H_2SO_4) as the titrant (Fig. 1e). The strong CO_2 signal from the Cu electrode (blue curve in Fig. 1e, equivalent to 0.035 mmol or 2.567 mg Li_2CO_3) in a Cu||NMC cell (representing a Li||NMC full cell) indicates substantial cross-talk (top of Fig. 1d). Cu was used in place of Li for safety reasons (see methods). In contrast, for d-LFP||NMC (i.e., the cathode half-cell), in which CO and CO_2 production was established (Fig. 1c), no cross-talk conversion into Li_2CO_3 occurred (bottom of Fig. 1d), thus resulting in no signal (gray curve in Fig. 1e). To establish a baseline, fresh Cu and delithiated LFP electrodes were also titrated, and no CO_2 signals were observed from these electrodes (Figs. S4c and S4d).

The features in the *in situ* volume plot for the Li||NMC full cell (Fig. 1b) illustrate the time-dependence of the aforementioned processes. First, *in situ* measurements for the cathode half-cell reveal that gas

evolution at the cathode occurs during the first cycle and levels off within the next cycle (Fig. S5, green curve). Similarly in the full cell (Fig. 1b, magenta curve), following a relatively small initial increase in volume—indicating CO and CO_2 gas production—during the first cycle, the volume levels off for several cycles. Notably, the onset of cathode gas evolution for DME on NMC811 occurs at approximately 4.18 V (vs. Li/Li^+), which is comparable to that for carbonate solvents on NMC811[34]. The ensuing gradual decrease in volume shown in Fig. 1b may reflect the consumption of CO and CO_2 at the anode via cross-talk, which was not observed in the cathode half-cell (Fig. S5). Some of the cathode gases may also dissolve into the electrolyte at the elevated experimental temperatures, but the effects are expected to be minor since the volume remains relatively constant in the cathode half-cell (Fig. S5). At about 5 cycles in (~ 3000 min), gas production (primarily CH_4) is anode-driven and steeply rises.

Gas Evolution at Cathode

Figure 2a shows the normalized volume fractions of gases produced at 60°C in d-LFP||NMC cathode half-cells when the LiFSI/DME electrolyte concentration was varied between 2–5 M. The volume of gas produced decreases with increasing LiFSI concentration. Holding the concentration constant at 4 M LiFSI/DME (Fig. 2b), the gas volume increases with increasing temperature over a range of 45–70°C. For all conditions, CO and CO_2 comprise of ~ 98% of the gas produced (Tables S3 and S4).

The reaction mechanisms for CO and CO_2 formation were investigated by first-principles simulation. The production of CO and CO_2 both result from DME oxidation at the NMC cathode, which follows two exergonic pathways (Fig. 2c). In both pathways, DME first adsorbs onto the NMC surface via interactions between the DME oxygen (O) and the transition metal (TM) atoms. Following the dark green pathway, after two successive dehydrogenations of a methyl end group, a DME C–O bond is cleaved to give an O = CH· radical, which then further loses a hydrogen (H) to a surface O atom to yield CO. The production of CO_2 (light green pathway) also begins with the dehydrogenation of a methyl end group. The methyl C then becomes associated with a surface O, leading to the extraction of the O atom from the NMC lattice. This O is incorporated into the DME structure while another H is lost to the surface. A C–O bond then breaks to give an O = C–O· radical. A final dehydrogenation step yields CO_2.

The decrease in the normalized gas volume (mL/Ahžh) with increasing LiFSI concentration shown in Fig. 2a can be attributed to several factors. First, decreasing the DME (reactant) concentration reduces the reaction rate, thus slowing gas production. The corresponding increase in the FSI^- concentration promotes the formation of a passivating cathode electrolyte interphase (CEI) at the NMC surface, which hinders oxidation reactions.[35,36] The polycrystalline NMC particles in a 5 M sample also exhibited less microcracking than for a lower electrolyte concentration (compare Figs. S6b and S6c). Since microcracks can form when interfacial side reactions erode the crystal surface,[37] more severe microcracking at a lower concentration may be indicative of an increased rate of DME reaction with the cathode surface, which then leads to more rapid gas production. A corresponding increase in the cathode thickness (Fig. S7) was also observed, which may result from reaction-induced deformations

such as microcracking. In contrast, the cathode thickness remains essentially unchanged from a fresh NMC electrode for the higher concentration (5 M) sample.

The increase in normalized volume with temperature (Fig. 2b) suggests the reaction is thermally activated, meaning the reaction rate increases with a rise in kinetic energy and the frequency of molecular collisions at higher temperatures. For a given concentration, a higher rate of DME decomposition results in a relatively larger volume of CO and CO_2 produced during the same experimental time window.

Gas Evolution at Anode

The dominant gas species in Li||LFP anode half-cells with varying electrolyte concentrations (2–5 M LiFSI/DME, Fig. 3a) and temperatures (45–70°C, Fig. 3b) is consistently CH_4 (~ 96–98%, Tables S5 and S6). The time dependence of the anode gas evolution is shown in Figs. 3c and 3d, with arrows indicating the onset times at which volume surges were observed. At the lowest 2 M concentration, the onset of gas evolution begins earliest (Fig. 3c, after 2 cycles), consistent with the most rapid gas generation and hence largest normalized volume of gas produced (Fig. 3a, ~ 0.6 mL/Ahžh). At the highest 5 M concentration, no onset point was observed (Fig. 3c) and no gas was detected over the experimental time window (Fig. 3a). The results in Fig. 3d similarly complement Fig. 3b, with earlier onset points at higher temperatures corresponding to larger normalized gas volumes produced.

To gain insights into the cell conditions before and after the onset point, the electrolyte content was measured at various cycles for a 4 M sample at 60°C using our recently developed electrolyte consumption analysis method.[33] As shown in Fig. 3e, the masses of both LiFSI (circles) and DME (squares) decrease with cycle number. The consumption of LiFSI is more rapid (steeper slope), leading to an overall decrease in the electrolyte concentration (triangles). A linear decrease in both LiFSI and DME over 15 cycles suggests that the rate of electrolyte consumption at the anode is unchanged before and after the onset point (at cycle 4). However, the results in Figs. 3c and 3d suggest that electrolyte decomposition does not produce gaseous species before the onset point but results in gaseous species afterwards. To understand this disparity surrounding the onset point, the DME decomposition pathways were calculated using first-principles simulation, as illustrated in Figs. 3g-i.

In Step 1 (Fig. 3g), DME adsorbs onto the Li surface. In the less exergonic pathway (pink, ΔG = − 2.69 eV), one of the C–O bonds in the ethane backbone is cleaved, resulting in two surface-bound species, a methoxy (Li–OCH_3) and a methoxyethyl (Li–$C_2H_4OCH_3$, highlighted in green) structure. In the second pathway (dark pink, ΔG = − 3.58 eV), the cleavage of the methoxy C–O bond generates a methyl group, which reacts with surface Li to form methyllithium ($LiCH_3$, highlighted in light orange). $LiCH_3$ can theoretically react with another DME, as shown in Step 2A (Fig. 3h), to produce CH_4 gas, the major gas species observed. However, the depletion of an additional DME molecule in this reaction is expected to alter the DME consumption rate at the onset point, contrary to the linear decrease over cycle number

observed experimentally (Fig. 3e). Alternatively, as shown in Step 2B (Fig. 3i), $LiCH_3$ can react with the methoxyethyl ($Li–C_2H_4OCH_3$) also produced in Step 1 to form CH_4 gas. This reaction does not involve any additional DME. Furthermore, the calculated activation energy of this pathway is 20% lower (0.88 vs. 1.14 eV). Thus, both theoretical and empirical results suggest that Step 2A does not occur, and only Step 2B occurs, with the two highlighted products from Step 1 reacting to produce CH_4.

To determine the trigger for CH_4 gas production and thus the onset point, a Li||LFP cell with 4 M LiFSI/DME was cycled at 60°C with 3.6 mmol/L of externally added $LiCH_3$ (compared to $LiCH_3$ formed *in situ* during cycling). The onset of gas evolution shifted forward, from cycle 4 to cycle 3 (Fig. 3f), suggesting that when $LiCH_3$ was abundant, the threshold $LiCH_3$ concentration was more rapidly reached and hence Step 2B proceeded earlier. In the presence of a large excess of $LiCH_3$, gas production began immediately (Fig. S8a). The linear consumption of DME and the reaction rate dependence on $LiCH_3$ concentration provide evidence for the pathway involving only Steps 1 and 2B. In other words, nongaseous $Li–C_2H_4OCH_3$ and $LiCH_3$ are first produced (Step 1, Fig. 3g). Then, once the $LiCH_3$ concentration accumulates to a threshold value, Step 2B (Fig. 3i) occurs, triggering the production of CH_4 gas, which manifests as the onset point.

It should be noted that while $LiCH_3$ produced at the anode can react with oxidation species that cross-talk from the cathode,[29,30,38,39] such as CO_2,[40] these pathways have limited effects on the experimental results. Comparison of gas evolution in Li||NMC (containing oxidation species, Fig. S9b) and Li||LFP (no oxidation species, Fig. S9a) cells cycled at 60°C with 4 M LiFSI/DME revealed that the onset point of gas evolution is only delayed by about one cycle in Li||NMC. In the Li||LFP cell, all $LiCH_3$ produced in Step 1 contributes to reaching the threshold level for CH_4 production. In contrast, in the Li||NMC cell, some $LiCH_3$ reacts with the oxidation species, delaying the buildup of $LiCH_3$ to reach threshold levels and hence produce CH_4 gas. Nonetheless, these reactions only delay the onset by one cycle, with minimal impact on the timing of the onset point.

Considering the anode half-cell only, the increasing delay in the onset point of CH_4 production with increasing LiFSI/DME concentration is the result of several factors, including the reduced concentration of DME and changes in the solvation structures. Simulation results (Fig. S10) for the Step 1 DME reduction at the anode show that the activation energies for conversion into $LiCH_3$ or $LiOCH_3$ intermediates (Fig. 3g, dark pink and pink pathways, respectively) are both higher for higher concentrations. Specifically, the activation energy for $LiCH_3$ formation increases from 0.69 to 0.88 eV (Figs. S10a-b), and for $LiOCH_3$ formation, from 0.58 to 0.75 eV (Figs. S10c-d). Thus, the rate of gas production and the gas volume decreases with increasing concentration. Note that for both pathways, the FSI^- anion is found in the first Li solvation shell at higher concentrations (Figs. S10b and S10d) and not in lower concentrations (Figs. S10a and S10c).

The shifting of the onset points to earlier times with increasing temperature at a given electrolyte concentration is, like the case for the cathode, a result of increased energy and frequency of molecular collisions leading to increased reaction rate. In this case, the accelerated reaction is the decomposition of DME to produce CH_4.

Electrolyte Engineering to Suppress Gas Evolution

Given that gas evolution stems primarily from CH_4 production at the anode, inhibiting the CH_4 reaction pathway should significantly reduce full cell gas generation. Furthermore, in practical applications, cathode gases can be efficiently removed after a formation cycle since they are only generated during the first cycle. In a cell treated in this manner, the effects of cross-talk can be avoided altogether and only anode gas production necessitates treatment.

When using the standard 4 M LiFSI/DME electrolyte (Fig. 4a), referred to as a high concentration electrolyte (HCE) due to its high concentration of the Li salt, CH_4 is derived from the terminal methyl group of the DME solvent (Figs. 3g-i). After only 20 cycles at 60°C, significant swelling of the Li||NMC cell was observed (see side and top views in Fig. 4a).

As mentioned above, the formation of the $Li–C_2H_4OCH_3$ and $LiCH_3$ intermediates that react to produce CH_4 is less kinetically favorable (higher activation energy) at higher concentrations of LiFSI/DME. While it is not pragmatic to indefinitely increase the LiFSI/DME concentration due to the associated costs of LiFSI and impractically high viscosities, a localized high concentration electrolyte (LHCE, Fig. 4b) can elevate the local LiFSI concentration, thus increasing the relative proportion of DME solvation structures that correspond to those with higher activation barriers, without actually adding significantly more LiFSI. The non-Li solvating diluent used for the LHCE shown in Fig. 4b is 1,1,2,2-tetrafluoroethyl-2,2,3,3-tetrafluoropropyl ether (TTE).[35] For this LHCE system, no gas was generated for over 150 cycles at 60°C, i.e., the pouch cell remains flat (Fig. 4b).

Another option is to replace the terminal methyl CH_3 groups in DME with fluorinated groups, eliminating the CH_4 source altogether. For example, the fluorinated ether electrolyte (FEE), 2-[2-(2,2-difluoroethoxy)ethoxy]-1,1,1-trifluoroethane (F5DEE, Fig. 4c),[41] terminates with difluoromethyl CF_2 and trifluoromethyl CF_3 groups. Since the critical intermediate $LiCH_3$ cannot be formed from F5DEE, no CH_4 should be generated. As observed in Fig. 4c, no gas was generated for over 120 cycles at 60°C.

Besides a reduction in gas generation, both LHCE and FEE exhibited improved capacity retention (Fig. 4d), with cycle lives of about 300 cycles for LHCE (magenta) and 120 cycles for FEE (blue) at 60°C. However, despite these favorable results, the LHCE and FEE systems exhibit poor rate performances (Fig. 4e) compared to the original HCE. This likely originates from their much lower ionic conductivities (Fig. 4f). These limitations significantly hinder their practical application in high power applications such as eVTOL, where maintaining high rate performance is not only critical for fulfilling take-off and landing

requirements, but also the capacity to respond to emergency situations and guarantee safety.[24,27,42] Thus, while the two electrolytes show promise, their poor rate performances render them inadequate for real-world applications. A more robust method was needed to simultaneously satisfy gas evolution and rate requirements. To achieve this, we turn our attention from the electrolyte to the other contributor in the anode-interfacial reactions, the anode itself.

Anode Activation to Suppress Gas Evolution

The thick native passivation film that forms on the surface of fresh, untreated Li metal, shown schematically as a brown film on the gray Li surface in Fig. 5a, is lithiophobic. Thus, metallic Li (pale green, Fig. 5b), deposits only from the more lithiophilic defects (mauve stripes in Figs. 5a-b) in this passivation film. Due to the limited number of defect sites, metallic Li tends to grow continuously from these sites, forming dendrites.[43,44] Dendritic Li, with their large surface areas, are highly susceptible to interfacial chemical reactions, leading to substantial electrolyte consumption, severe gas generation, and poor cycling performance. However, if the native Li anode surface is activated via stripping (Fig. 5c), it is possible to obtain an extended array of pits in which fresh, metallic Li is exposed.[43,45] A thin passivation layer (dark green, Fig. 5c) forms in these newly created pits through reactions between the metallic Li and the electrolyte; these newly formed surfaces remain relatively lithiophilic and conducive to Li deposition. Given the abundance of pits, and thus Li deposition sites, Li deposits in a more two-dimensional manner across the surface, in particle or globule form (Fig. 5d), instead of three-dimensionally away from the anode surface.[43,44] In other words, the activated anode is less susceptible to dendrite formation.

The morphologies of untreated and activated anodes in Li||NMC cells with 4 M LiFSI/DME cycled at 60°C were investigated using SEM imaging. The untreated anode surface (Fig. 5e) yielded roughly four nucleation sites (Fig. 5f) within an approximately 0.2 mm^2 region. Shown in Fig. 5f is Li deposition following an initial charge to 10% SOC. In comparison, for a similar sized region, the activated, or pre-stripped, anode contains about 80 pits (Fig. 5g), 20 times the number of potential Li nucleation sites. These pits were confirmed to be Li nucleation sites as Li deposited within them upon initially charging the activated anode to 10% SOC (Fig. 5h).

When Li deposition was allowed to continue to 100% SOC, differences in the morphology of the deposited Li became apparent. For the untreated anode, Li metal grew continuously from the sparse defect sites, forming narrow and long dendrites (Fig. 5i, 100% SOC). After 8 cycles, the cross-sectional image of the anode (Fig. 5j, 0% SOC) revealed a surface covered with a porous solid electrolyte interphase (SEI) layer, also known as the residual SEI (rSEI),[8,46] with a thickness of close to 30 μm. On the activated anode, a comparable amount of Li deposition resulted in large, globular Li particles formed from the numerous nucleation sites (Fig. 5k, 100% SOC), a distinctly different morphology compared to the elongated dendrites. The rSEI formed on the activated anode (Fig. 5l), with a thickness of less than 1 μm, is 30 times thinner than that formed on the untreated anode.

In addition to the differences in surface morphology and SEI thicknesses, there were also significant changes in the battery performance and gas evolution characteristics. The lower specific area of the deposited Li particles for the activated anode, compared to that of the Li dendrites on the untreated anode, resulted in fewer interfacial reactions, thus impacting electrolyte consumption, gas generation, and ultimately, cycling performance.

For the same concentration of electrolyte (4 M LiFSI/DME) at the same temperature (60°C), the LiFSI and DME contents of the activated sample decreased much less rapidly with cycling compared to the untreated sample. This is shown in Fig. 5m, in which the slopes of the linear fits to the masses for the activated sample (blue) are less steep relative to the untreated sample (magenta). The overall concentration (Fig. 5n) of the electrolyte in the activated sample also only moderately decreased from 4 M to 3.9 M after 15 cycles, compared to a more drastic decrease to 2.9 M for the untreated sample.

The consequences of fewer interfacial reactions, as evidenced by the reduced electrolyte consumption in the activated anode sample, include improved cycling performance and delayed gas generation. Figure 5o shows that the untreated sample (magenta) had only undergone 30 cycles when the capacity plunged from an initial capacity of roughly 150 mAh to below 100 mAh. In contrast, the activated sample (blue) completed close to 160 cycles before the capacity finally decayed to 100 mAh, which is an extension of the cycle life by over a factor of five. Concurrently, gas evolution was delayed by at least a factor of nine. The onset point of the untreated sample (Fig. 5p, magenta) occurs after 5 cycles, followed by abrupt and substantial gas generation. However, for the activated sample (blue), gas evolution begins gradually after 45 cycles.

By solely controlling the morphology of Li deposition on the anode surface to reduce the surface area of deposited Li, interfacial reactions were successfully curbed, enabling improvements in various indicators of battery performance. Without changing the electrolyte system nor the cycling conditions, mitigated electrolyte consumption, better cycling performance, and delayed gas generation were all achieved. In other words, anode activation offers a universal means of enhancing the safety and cycling of lithium metal batteries. To fully explore the potential of the method, additional studies with other electrolytes and cycling conditions are warranted. Improving battery performance involves a diverse toolbox of strategies, and synergistic utilization of this form of anode activation with rationally designed materials and protocols, even other means of anode modification, stands to fully harness the potential of lithium metal batteries.

Conclusion

In this work, gas evolution in ether-based lithium metal batteries (LMBs) was quantified and its mechanistic underpinnings were elucidated through experimental and computational studies. Based on the finding that the primary source of gas generation is DME decomposition at the anode and with insights from the corresponding simulated mechanisms, two strategies targeting the solvent-anode interfacial reductions were implemented. Reduced gas evolution and longer cycle lives were obtained

with both electrolyte engineering and anode activation strategies, but with a significant decline in rate performance for the alternative electrolytes tested. However, for the anode activation method, stellar rate performance was still possible.

These results highlight the importance of developing a fundamental understanding of the problem (i.e., mechanism of gas evolution) and evaluating the pertinent engineering solutions against industrially relevant metrics using state-of-the-art battery prototypes. LMB research in recent years often focused on enhancing the cycle life[9–17] without holistic assessment of the product characteristics required for practical applications. Aviation batteries, such as those used in electric vertical take-off and landing (eVTOL) aircraft, must simultaneously exhibit excellent rate performance under room temperature and minimal gas generation at elevated temperatures to support the demands of take-off and landing operations with high reliability.[24,25,47] Thus, an improvement in cell safety (e.g., dendrite and gas generation suppression) without compromising on cell performance for the anode activation approach using 4 M LiFSI/DME electrolyte presents a significant step toward achieving such a goal.

While the anode activation approach offers notable benefits, there remains the concern that it could potentially damage the cathode's structural integrity, as Li anode stripping requires the cathode to accept the excess Li ions and overlithiate. Future research directions may include exploring synthesizing Li-deficient NMC cathodes or using sulfur cathodes, which can accommodate more Li ions without excessive strain. Furthermore, other strategies and electrolyte designs should also be evaluated against the standards laid out here. Only through such a product-oriented research methodology, can academic efforts serve to advance the viability of LMB commercialization, ultimately encouraging electrification efforts and reducing the societal carbon footprint.

Methods

Materials and Cells

LiFSI (99.99%, Kaixin Co., Ltd), DME (99.95%, Guotai Co., Ltd), TTE (99.5%, Aladdin Co., Ltd), and F5DEE (99%, synthesized with the assistance of Sikang Chemical Co., Ltd.) were used for the electrolyte solutions. 2, 4 and 5 M LiFSI in DME (denoted as HCE), LiFSI-1.2DME-3TTE (by mole ratio, denoted as LHCE), and 1.2 M LiFSI in F5DEE (denoted as FEE) were prepared and injected (2.1 g/Ah for all samples) into corresponding dry cells in a dry room with a relative humidity of <1%. Cell assembly and teardowns were also performed in a dry room. The Li anodes consisted of 13 μm thick Cu foils with 50 μm of Li on either one side or both sides. The NMC used is the 811 type ($LiNi_{0.8}Mn_{0.1}Co_{0.1}O_2$, mono- and poly-crystalline mix, Rongbai Co., Ltd). Prior to cycling, samples were set to 0.4 MPa initial pressure using a custom-designed clamp and equilibrated at the desired temperature (45, 60, and 70 °C) for 2 h.

Li||NMC and Li||LFP

The Li||NMC full cells and the Li||LFP anode half-cells were fabricated in a CATL pilot line with double-sided NMC and LFP electrodes, with design capacities of 140 mAh (cathode areal capacity of 3.37 mAh/cm^2) and 150 mAh (3.61 mAh/cm^2), respectively. After electrolyte injection, they were cycled at 0.2 C (charge)-0.5 C (discharge) between 0-100% SOC (28–70 mA, 2.8–4.3 V for Li||NMC and 30–75 mA, 2.8–3.65 V for Li||LFP) without any formation cycles following a conventional constant current-constant voltage (CC-CV) protocol with a cutoff current of 0.1 C (14 mA for Li||NMC and 15 mA for Li||LFP). The battery cycler used was a Neware CT-4008Tn-5V6A-S1 (Neware Technology Ltd., Shenzhen, China).

d-LFP||NMC

Preparation of the d-LFP||NMC cathode half-cell involves multiple steps. First, a Li||LFP cell with 4 M LiFSI/DME electrolyte was fabricated using a Li anode and a single-sided LFP electrode with a design capacity of 75 mAh (3.61 mAh/cm^2). This cell was subjected to 1 cycle at 0.1 C-0.1 C and then charged at 0.1 C for 10 hours to produce a “Li vacancy” (specifically, 70 mAh) while keeping the cell voltage within a voltage plateau. The delithiated LFP electrode was then extracted, soaked for 10 min and rinsed in DME, and used as the “anode” for the d-LFP||NMC cathode half-cell. The NMC electrode was designed with a capacity of 40 mAh (1.92 mAh/cm^2) to enable cycling at the plateau voltage of LFP. The d-LFP||NMC cells were injected with the appropriate concentration of LiFSI/DME electrolyte solutions and cycled at 0.2 C-0.5 C (CC-CV with a cutoff current of 0.1 C) between 0-100% SOC (-0.63 to 0.87 V vs. $E_{LFP\ plateau}$ = 3.43 V) without any formation cycles.

d-LFP||LFP

Fabrication of the d-LFP||LFP cell (used for testing LFP inertness) also first involved construction and cycling of a Li||LFP cell as described above for the d-LFP||NMC cell. The delithiated LFP electrode, with a design capacity of 75 mAh (3.61 mAh/cm^2), was then used as the “anode” for the d-LFP||LFP cell. The other LFP electrode serving as the “cathode” is also single-sided, but designed with a capacity of 60 mAh. After injection of 4 M LiFSI/DME, the d-LFP||LFP cell was cycled at 0.2 C-0.5 C between 0-100% SOC (-0.63 to 0.22 V vs. $E_{LFP\ plateau}$ = 3.43 V) for 30 cycles at 60°C.

Cu||NMC and Cu||Li

The Cu||NMC and Cu||Li cells used for T-MS experiments were prepared with 13 μm thick Cu foils, double-sided NMC electrodes (design capacity of 140 mAh), and 13 μm thick Cu foils with 50 μm of Li on each side. Cu||NMC cells were cycled for 10 cycles at 60°C at 28 mA (charge)-100 mA (discharge) (CC-CV with a cutoff current of 14 mA) between 2.8–4.3 V. After that, a deep discharge was conducted to strip the remaining Li (7 mA to 2.8 V, 3.5 mA to 2.8 V, and 1 mA to 2.8 V, with 5 min rest between each step). Cu||Li cells were cycled for 10 cycles at 60°C. During the first cycle, 200 mAh of Li was deposited on the Cu electrode at 28 mA (charge) and 125 mAh of Li was stripped at 100 mA. For the following cycles, 125 mAh of Li was deposited and stripped at 28 mA and 100 mA, respectively. Finally, a deep discharge was conducted to strip the remaining Li from the Cu electrode (7 mA to -1 V, 3.5 mA to -1 V, and 1 mA to -1 V, with 5 min rest between each step).

Gas Volume Determination

Changes in the cell volume were determined using the Archimedes principle.[28] A fine wire was used to suspend a sample cell secured with metal clamps in a container of fluid. As the cell volume changes, the volume of fluid the cell displaces changes, thus resulting in changes in the buoyant force acting on the cell and ultimately the overall weight of the fluid-filled container.

For *ex situ* measurements (performed at 25°C), a beaker with 1000 ml of filtered water (18.2 MΩ•cm at 25°C, Thermo Scientific Barnstead NANOpure Water Purification System) was first tared on an analytical balance (Shimadzu, AUW200D). After submerging a suspended cell, the beaker system was weighed again. The volume of the immersed cell was calculated as the additional mass measured on the balance divided by the density of water (i.e., the volume of displaced water). The gas volume generated during cycling was determined by conducting measurements before and after cycling. Note, the cell tabs were insulated with tape to prevent short-circuiting. Normalized gas volumes were calculated as:

$$\mathrm{V_N}=\frac{\mathrm{V_{total}}}{\mathrm{C_d}\times\mathrm{t}}$$

where V_N is the normalized gas volume (mL/Ahžh), V_{total} is the total gas volume (mL), C_d is the design capacity (Ah), and *t* is the total cycling time (h).

In situ measurements were performed using an *in situ* battery gassing volume analyzer (Initial Energy Science & Technology, GVM2200). In this setup, the cell was submerged in silicone oil and volume changes were recorded in real time as the cells were cycled using a Neware BTS-5V1mA testing system (Neware Technology Ltd., Shenzhen, China). Cells tested at 45°C, 60°C and 70 $^{\circ}C$ were equilibrated for 4 h prior to testing.

Gas Component Determination

After a cell was cycled, the generated gases were sampled by puncturing the aluminum-plastic pouch with a syringe. The collected gas was injected into an Agilent 8890 gas chromatograph (GC) system with an inlet temperature of 120°C and a 10:1 split ratio. The argon carrier gas flow rate was set to 8 mL/min. Two columns were used in series: a 5 Å molecular sieve column (CP-Molsieve 5 Å; 25 m, 0.53 mm, 50 µm) and a PLOT column (HP-PLOT Q PT; 30 m, 0.53 mm, 40 µm). Following the columns are a thermal conductivity detector (TCD, Agilent) and a flame ionization detector (FID, Agilent). This set of columns and detectors enables clean detection of permanent gases (H_2, O_2, N_2, CO, CO_2) and light hydrocarbons (CH_4, C_2H_6, C_2H_4) in a single injection. The TCD sensitivity was optimal at an operation temperature of 220°C, a makeup flow rate of 5 mL/min, and a reference flow rate of 30 mL/min.

A custom gas mixture of known composition was used to determine the retention times for the gaseous compounds of interest and to perform signal calibration. The gas mixture was obtained from Jining Xieli Special Gas Co., Ltd and contains, by volume percent, 8.99% carbon dioxide, 8.98% carbon monoxide,

9.02% ethane, 8.93% ethylene, 0.497% acetylene, 9.02% propane, 8.99% propylene, 9.24% hydrogen, 0.633% oxygen, 8.99% methane, and 26.71% nitrogen.

Cross-Talk Validation: Indirect CO_2 Detection

To address why CO_2 was detected in the cathode half-cell but not the full cell, Li_2CO_3, the expected cross-talk product of CO_2 and the Li surface, was probed using titration-mass spectroscopy (T-MS). The reaction of Li_2CO_3 with the H_2SO_4 titrant is as follows:

$$Li_2CO_3 + H_2SO_4 \rightarrow Li_2SO_4 + H_2O + CO_2 \uparrow$$

In other words, if CO_2 produced at the cathode transfers to the anode to produce solid Li_2CO_3 (i.e., cross-talk), the resulting Li_2CO_3 on the extracted anode would react with H_2SO_4 to produce CO_2 gas, which can then be collected and measured by MS (Shanghai LingLu Instruments Co., Ltd., QAS 100). In cells where CO_2 is produced (as evidenced by GC) but no cross-talk occurs (e.g., d-LFP||NMC cell), no Li_2CO_3 would form at the anode, and hence no CO_2 would be detected by MS.

As a precaution, since Li reacts violently with H_2SO_4, the system with cross-talk was modeled with Cu||NMC (“full cell”), using Cu instead of Li. The system without cross-talk was modeled with d-LFP||NMC (cathode half-cell). Furthermore, deposited Li was stripped from the Cu and LFP electrodes prior to cell disassembly. The extracted electrode was titrated with 10 M H_2SO_4. A cycled Cu||Li cell, in which CO_2 was not produced during cycling, was tested as a control sample (Fig. S4b). Fresh Cu and d-LFP electrodes were also tested to check for background signals Figs. S4c and S4d).

A calibration equation for Li_2CO_3 was obtained through titration of a Li_2CO_3 standard sample (99.5%, Macklin Co., Ltd). Known masses of Li_2CO_3 were titrated and the resulting CO_2 signals were integrated, yielding a calibration curve (Fig. S4a). Thus, for a given value of an integrated CO_2 signal, the corresponding mass of Li_2CO_3 could be obtained.

Electrolyte Consumption Analysis

Electrolyte consumption analysis was performed to quantify the loss of LiFSI and DME with cycling. LiFSI was quantified using ion chromatography (IC) and DME by gas chromatography (GC). Both LiFSI and DME were extracted from the cell using an extraction agent. Hence, the complete method was termed extraction-gas and ion chromatography (E-G&IC).[33]

1. Preparation of Extraction Agent

An internal standard, 1,2-diethoxyethane (DEE, 99.9%, Aladdin Co., Ltd), was added to correct for matrix effects and sample loss during preparation for GC analysis. The internal standard was added to the sample along with diethylene glycol dimethyl ether (diglyme, 99.99%, Aladdin Co., Ltd), in the form of an extraction agent, which was prepared by dissolving 4 g of DEE in diglyme, and making up the solution to 200 mL in a volumetric flask. The extraction agent was sealed and stored for later use.

2. Electrolyte Extraction

A small cut was made in the cycled cell inside an argon-filled glovebox (H_2O < 0.1 ppm, O_2 < 0.1 ppm). After injecting 5 mL of the extraction agent, the cell was immediately re-sealed and gently shaken. The cell was allowed to rest under room temperature for 7 days for thorough extraction. The liquid content was then extracted from the cell and syringe filtered for further processing.

3. Ion Chromatography (IC) for Quantifying LiFSI

Six standard LiFSI solutions with 0, 25, 50, 100, 150, and 200 mg LiFSI were prepared by dissolving the respective amounts in 1000 mL of deionized water. 5 mL aliquots were analyzed with IC (Dionex Aquion RFIC, Thermo Scientific) to obtain the LiFSI peak area for each corresponding concentration. Linear regression was performed between the peak areas and LiFSI concentrations, forming a calibration curve (Fig. S11a).

Samples extracted from the cell were diluted with deionized water using a dilution factor of 200. A 5 mL aliquot of the diluted solution was measured with IC. The concentration of the diluted sample (c_{LiFSI}) was determined from the measured peak area (S_{LiFSI}):

$$S_{\mathrm{LiFSI}} = k_{\mathrm{LiFSI}} \times\ c_{\mathrm{LiFSI}}$$

where k_{LiFSI} is the slope of the calibration curve. To obtain the absolute mass of LiFSI (m_{LiFSI}) remaining in the cycled cell, the concentration of the diluted sample was multiplied by the dilution factor (DF = 200) and the volume of the extracted solution:

$$m_{\mathrm{LiFSI}} = c_{\mathrm{LiFSI}} \times\ 200 \times\ 5.245\ \mathrm{mL}$$

where 5.245 mL comes from 5 mL for the extraction agent and 0.245 mL for 0.3 g of 4 M LiFSI/DME.

4. Gas Chromatography (GC) for Quantifying DME

A standard solution was prepared by first adding 0.3 g of fresh electrolyte (4 M LiFSI/DME) to 5 mL of extraction agent. This solution was then diluted with diglyme with DF = 5. A 1.5 mL aliquot was measured with GC (Nexis GC-2030, Shimadzu). A response factor f_{DME} was calculated for DME using the known masses of DME and DEE ($m_{\mathrm{DME}},\ m_{\mathrm{DEE}}$) in the standard solution and the peak areas extracted from the GC measurement ($S_{\mathrm{DME}},\ S_{\mathrm{DEE}}$):

$$f_{\mathrm{DME}} = \frac{m_{\mathrm{DME}}/S_{\mathrm{DME}}}{m_{\mathrm{DEE}}/S_{\mathrm{DEE}}}$$

Samples extracted from the cell were diluted with diglyme with DF = 5. A 1.5 mL aliquot of the diluted solution was measured with GC. To obtain the absolute mass of DME ($m_{\mathrm{DME,\ exp}}$) remaining in the cycled cell, the ratio of the obtained peak areas ($S_{\mathrm{DME,\ exp}},\ S_{\mathrm{DEE,\ exp}}$) were multiplied by the mass of the DEE added ($m_{\mathrm{DEE,\ exp}}$) in the form of the extraction agent, and the response factor (f_{DME}):

$$m_{\mathrm{DME,\,exp}} = m_{\mathrm{DEE,\,exp}} \times f_{\mathrm{DME}} \times \frac{S_{\mathrm{DME,\,exp}}}{S_{\mathrm{DEE,\,exp}}}$$

First-Principles Simulation

Density functional theory (DFT) calculations were performed with the Vienna *ab initio* simulation package (VASP).[48,49] The generalized gradient approximation and Perdew-Burke-Ernzerhof functional within the DFT framework were applied to determine the electron exchange-correlation energies.[50] Transition metals were treated using the DFT + U augmented approach with U values of 4, 4.4, and 5 eV for Mn, Co, and Ni, respectively.[51] Weak interactions were accounted for with the DFT + D3 method with dispersion correction. All calculations were spin-polarized with a plane wave cutoff energy of 520 eV. Surface calculations were performed with a 2 x 2 x 1 Monkhorst-Pack k-point scheme. A 15 Å vacuum layer was introduced to avoid interactions between periodic slabs.

A five-layer slab of lithium (110) was used to investigate the DME reduction processes and a charged slab of NMC811 was used to investigate the DME oxidation processes. Geometric structural optimization was performed until the force on all atoms was less than 0.02 eV/Å, with an energy convergence criterion set to less than 10^{-5} eV/atom. Transition states were located using the climbing image nudged elastic band (CI-NEB)[52] and dimer methods[53], with only one imaginary vibrational frequency being identified for each transition state along the reaction coordinate.

The ground state molecular and ion geometries were optimized using the DFT method at the B3LYP/6-311G+(d, p) level. All DFT calculations were performed using the Gaussian 09 software package. The MD simulations were conducted using the GROMACS 2018 program.[54] The molecules and ions were described using the optimized potentials for liquid simulations all-atom (OPLS-AA) force field.[55] The partial charges on the atoms of the solvent were computed by fitting the molecular restrained electrostatic potential (RESP) at the atomic centers using the B3LYP/aug-cc-pVDZ basis set.[56] The simulation boxes were cubic with a side length of approximately 4 nm and contained different concentrations of LiFSI/DME, LiFSI-1.2DME-3TTE and 1.2 M LiFSI/F5DEE. During the simulations, the temperature was maintained at 333 K using a Nosé-Hoover thermostat with a relaxation time of 0.2 ps, and the pressure was controlled at 1 bar using a Parrinello-Rahman barostat with a relaxation time of 2.0 ps. From a total simulation duration of 40 ns, the last 20 ns were utilized for analysis.

Anode Activation

Li||NMC cells with 4 M LiFSI/DME were used for investigating the effects of anode activation. To activate the anode, the cell was discharged to 1.5 V at 25 ℃ using progressively smaller C-rates: 1 C (140 mA), 0.8 C (112 mA), 0.6 C (84 mA), 0.4 C (56 mA), 0.2 C (28 mA) and 0.1 C (14 mA), with a 5 min rest between each step. To determine the optimal cut-off voltage (i.e., 1.5 V), a series of potentiostatic discharge experiments was performed. The anode activated using 1.5 V was observed to simultaneously

support good cycling performance and minimize gas evolution. Results for all voltages tested (1.3–2.1 V) are shown in Fig. S12, along with comments on why voltages both above and below 1.5 V were not suitable.

Activated and non-activated samples were subjected to three test conditions at 60 ℃: charging to 10% SOC at 0.2 C (28 mA), charging to 100% SOC at 0.2 C (28 mA), and discharging to 0% SOC after 8 cycles (0.2 C-0.5 C, 28 mA-70 mA).

SEM Characterization

Scanning electron micrographs of the anode samples were acquired with an ultrahigh resolution cold-field emission scanning electron microscope (SEM, Hitachi SU8600). Prior to imaging, anodes extracted from cycled cells were washed and dried thrice in a dry room, with a 10 min DME soak each time. To prepare a cross-sectional sample, a long, thin strip of washed anode was quenched in liquid nitrogen for 60 min, then swiftly split on a stainless-steel blade to expose a clean cross-section on each of the split pieces.

Extracted cathode samples were washed and dried in the same manner as the anode. A small piece of the sample was cut and transferred to an ion beam cross-section polisher (CP, Hitachi ArBlade 5000) under dry atmosphere and polished at room temperature under inert conditions to expose a clean cross-section for imaging.

Ionic Conductivities

Ionic conductivities were measured using a benchtop conductivity meter (LeiCi, DDSJ-318).

Declarations

Author Information

Corresponding Authors

Hansen Wang https://orcid.org/0000-0002-6738-1659

Xiaonan Luo https://orcid.org/0000-0002-0555-5481

Chuying Ouyang https://orcid.org/0000-0001-8891-1682

Authors

Yuchun Wang https://orcid.org/0009-0000-6141-7318

Samantha T. Hung https://orcid.org/0000-0001-9448-0962

Acknowledgements

X. L. acknowledges support from Fujian Provincial Natural Science Foundation of China under Grant No. 2024J08378. H. W. acknowledges support from the National Natural Science Foundation of China under Grant No. 22209085, and the support from Fujian Provincial Natural Science Foundation of China under Grant No. 2024J010048. C. O. acknowledges support from the National Natural Science Foundation of China under Grant No. 51962010. This work is also supported by funds from Contemporary Amperex Technology Co., Limited (CATL). We would like to extend our gratitude to Xiangen Cao and other team members at Sikang Chemical Co., Ltd. for their invaluable assistance in the synthesis of F5DEE.

Author contributions

Y.W., X.L., H.W., N.L. and C.O. conceived the idea and designed experiments. Y.C., S.T.H. and Z.C. performed the experiments and analyzed the data. J.S., L.B., E.W. and J.L. performed first-principles simulations. H.L. facilitated the quantitative measurements on gas generations. S.T.H., Y.W. co-wrote the manuscript with revisions from U.U., X.L., H.W., N.L. and C.O.

Competing interests

All authors are employed by Contemporary Amperex Technology Co., Limited (CATL).

Data availability

All data supporting the findings of this study are included in the Article and its Supplementary Information.

References

1. Aiken, C. P. *et al.* A Survey of In Situ Gas Evolution during High Voltage Formation in Li-Ion Pouch Cells. *J. Electrochem. Soc.* **162**, A760 (2015).
2. Liu, P. *et al.* Revealing Lithium Battery Gas Generation for Safer Practical Applications. *Adv. Funct. Mater.* **32**, 2208586 (2022).
3. Tarascon, J.-M. & Armand, M. Issues and challenges facing rechargeable lithium batteries. *Nature* **414**, 359–367 (2001).
4. Lin, D., Liu, Y. & Cui, Y. Reviving the lithium metal anode for high-energy batteries. *Nat. Nanotechnol.* **12**, 194–206 (2017).
5. Albertus, P., Babinec, S., Litzelman, S. & Newman, A. Status and challenges in enabling the lithium metal electrode for high-energy and low-cost rechargeable batteries. *Nat. Energy* **3**, 16–21 (2018).
6. Chen, S., Dai, F. & Cai, M. Opportunities and Challenges of High-Energy Lithium Metal Batteries for Electric Vehicle Applications. *ACS Energy Lett.* **5**, 3140–3151 (2020).
7. Yang, X.-G., Liu, T., Ge, S., Rountree, E. & Wang, C.-Y. Challenges and key requirements of batteries for electric vertical takeoff and landing aircraft. *Joule* **5**, 1644–1659 (2021).

8. Wang, H. *et al.* Rate-Dependent Failure Mechanisms and Mitigating Strategies of Anode-Free Lithium Metal Batteries. *ACS Appl. Mater. Interfaces* **15**, 12967–12975 (2023).
9. Qian, J. *et al.* High rate and stable cycling of lithium metal anode. *Nat. Commun.* **6**, 6362 (2015).
10. Fan, X. *et al.* Highly fluorinated interphases enable high-voltage Li-metal batteries. *Chem* **4**, 174–185 (2018).
11. Suo, L. *et al.* Fluorine-donating electrolytes enable highly reversible 5-V-class Li metal batteries. *Proc. Natl. Acad. Sci.* **115**, 1156–1161 (2018).
12. Liu, J. *et al.* Pathways for practical high-energy long-cycling lithium metal batteries. *Nat. Energy* **4**, 180–186 (2019).
13. Weber, R. *et al.* Long cycle life and dendrite-free lithium morphology in anode-free lithium pouch cells enabled by a dual-salt liquid electrolyte. *Nat. Energy* **4**, 683–689 (2019).
14. Yu, Z. *et al.* Molecular design for electrolyte solvents enabling energy-dense and long-cycling lithium metal batteries. *Nat. Energy* **5**, 526–533 (2020).
15. Chen, Y. *et al.* Steric Effect Tuned Ion Solvation Enabling Stable Cycling of High-Voltage Lithium Metal Battery. *J. Am. Chem. Soc.* **143**, 18703–18713 (2021).
16. Wang, H. *et al.* Dual-Solvent Li-Ion Solvation Enables High-Performance Li-Metal Batteries. *Adv. Mater.* **33**, 2008619 (2021).
17. Wang, H. *et al.* Liquid electrolyte: The nexus of practical lithium metal batteries. *Joule* **6**, 588–616 (2022).
18. Li, Z. *et al.* Non-polar ether-based electrolyte solutions for stable high-voltage non-aqueous lithium metal batteries. *Nat. Commun.* **14**, 868 (2023).
19. Park, M. S. *et al.* A highly reversible lithium metal anode. *Sci. Rep.* **4**, 3815 (2014).
20. Jie, Y., Ren, X., Cao, R., Cai, W. & Jiao, S. Advanced Liquid Electrolytes for Rechargeable Li Metal Batteries. *Adv. Funct. Mater.* **30**, 1910777 (2020).
21. Gan, L. *et al.* Comparative study of thermal stability of lithium metal anode in carbonate and ether based electrolytes. *J. Power Sources* **551**, 232182 (2022).
22. Xiang, Y. *et al.* Gas induced formation of inactive Li in rechargeable lithium metal batteries. *Nat. Commun.* **14**, 177 (2023).
23. Nie, Q. *et al.* Research Progress of Liquid Electrolytes for Lithium Metal Batteries at High Temperatures. *Small* **19**, 2302690 (2023).
24. Clarke, M. A. & Alonso, J. J. Forecasting the Operational Lifetime of Battery-Powered Electric Aircraft. *J. Aircr.* **60**, 47–55 (2023).
25. Bills, A. *et al.* A battery dataset for electric vertical takeoff and landing aircraft. *Sci. Data* **10**, 344 (2023).
26. Zhao, C., Mazo, J. R. & Verstraete, D. Optimisation of a liquid cooling system for eVTOL aircraft: Impact of sizing mission and battery size. *Appl. Therm. Eng.* **246**, 122988 (2024).

27. Wu, Z., Lian, W., Chen, B. & Zheng, C. Research on battery heat generation characteristics and thermal management system applied to a typical eVTOL. *Appl. Therm. Eng.* **257**, 124187 (2024).
28. Aiken, C. P. *et al.* An apparatus for the study of in situ gas evolution in Li-ion pouch cells. *J. Electrochem. Soc.* **161**, A1548 (2014).
29. Ellis, L. D. *et al.* Quantifying, Understanding and Evaluating the Effects of Gas Consumption in Lithium-Ion Cells. *J. Electrochem. Soc.* **164**, A3518 (2017).
30. Bharti, A., Deb, D., Achutharao, G. & Bhattacharyya, A. J. CO_2 Crossover to the Li Anode and Its Implications on the Solid Electrolyte Interphase Composition in a Rechargeable Li–CO_2 Battery. *J. Phys. Chem. C* **128**, 11543–11551 (2024).
31. Cotton, F. A., Wilkinson, G. & Gaus, P. L. *Basic inorganic chemistry*. (Wiley India, 2004).
32. Zhang, H. *et al.* Titration Mass Spectroscopy (TMS): A Quantitative Analytical Technology for Rechargeable Batteries. *Nano Lett.* **22**, 9972–9981 (2022).
33. Wang, H. *et al.* Quantifying Interfacial Reactions in Lithium Metal Batteries for a New Paradigm of Long-Cycling Electrolyte Designs. Preprint at https://doi.org/10.21203/rs.3.rs-3855314/v1 (2024).
34. Jung, R., Metzger, M., Maglia, F., Stinner, C. & Gasteiger, H. A. Chemical versus Electrochemical Electrolyte Oxidation on NMC111, NMC622, NMC811, LNMO, and Conductive Carbon. *J. Phys. Chem. Lett.* **8**, 4820–4825 (2017).
35. Ren, X. *et al.* Enabling High-Voltage Lithium-Metal Batteries under Practical Conditions. *Joule* **3**, 1662–1676 (2019).
36. Ren, X. *et al.* High-Concentration Ether Electrolytes for Stable High-Voltage Lithium Metal Batteries. *ACS Energy Lett.* **4**, 896–902 (2019).
37. Han, D., Weng, J., Zhang, X., Tong, Q. & Zhu, M. Review—Revealing the Intercrystalline Cracking Mechanism of NCM and Some Regulating Strategies. *J. Electrochem. Soc.* **169**, 040512 (2022).
38. Metzger, M., Strehle, B., Solchenbach, S. & Gasteiger, H. A. Origin of H_2 Evolution in LIBs: H_2O Reduction vs. Electrolyte Oxidation. *J. Electrochem. Soc.* **163**, A798–A809 (2016).
39. Harris, O. C., Lee, S. E., Lees, C. & Tang, M. Review: mechanisms and consequences of chemical cross-talk in advanced Li-ion batteries. *J. Phys. Energy* **2**, 032002 (2020).
40. Kaufmann, E., Sieber, S. & Schleyer, P. V. R. Carboxylation of lithium compounds: ab initio mechanisms. *J. Am. Chem. Soc.* **111**, 4005–4008 (1989).
41. Yu, Z. *et al.* Rational solvent molecule tuning for high-performance lithium metal battery electrolytes. *Nat. Energy* **7**, 94–106 (2022).
42. Courtin, C., Mahseredjian, A., Dewald, A. J., Drela, M. & Hansman, J. A Performance Comparison of eSTOL and eVTOL Aircraft. in *AIAA AVIATION 2021 FORUM* (American Institute of Aeronautics and Astronautics, 2021). doi:10.2514/6.2021-3220.
43. Huang, Y., Pan, R., Rehnlund, D., Wang, Z. & Nyholm, L. First-Cycle Oxidative Generation of Lithium Nucleation Sites Stabilizes Lithium-Metal Electrodes. *Adv. Energy Mater.* **11**, 2003674 (2021).

44. Frenck, L., Sethi, G. K., Maslyn, J. A. & Balsara, N. P. Factors That Control the Formation of Dendrites and Other Morphologies on Lithium Metal Anodes. *Front. Energy Res.* **7**, 115 (2019).
45. Rehnlund, D., Ihrfors, C., Maibach, J. & Nyholm, L. Dendrite-free lithium electrode cycling via controlled nucleation in low LiPF6 concentration electrolytes. *Mater. Today* **21**, 1010–1018 (2018).
46. Wang, H. *et al.* Efficient Lithium Metal Cycling over a Wide Range of Pressures from an Anion-Derived Solid-Electrolyte Interphase Framework. *ACS Energy Lett.* **6**, 816–825 (2021).
47. He, J. *et al.* Key technologies and upgrade strategies for eVTOL aircraft energy storage systems. *J. Energy Storage* **103**, 114402 (2024).
48. Kresse, G. & Furthmüller, J. Efficient iterative schemes for *ab initio* total-energy calculations using a plane-wave basis set. *Phys. Rev. B* **54**, 11169–11186 (1996).
49. Kresse, G. & Furthmüller, J. Efficiency of ab-initio total energy calculations for metals and semiconductors using a plane-wave basis set. *Comput. Mater. Sci.* **6**, 15–50 (1996).
50. Perdew, J. P., Burke, K. & Ernzerhof, M. Generalized Gradient Approximation Made Simple. *Phys. Rev. Lett.* **77**, 3865–3868 (1996).
51. Grimme, S., Antony, J., Ehrlich, S. & Krieg, H. A consistent and accurate *ab initio* parametrization of density functional dispersion correction (DFT-D) for the 94 elements H-Pu. *J. Chem. Phys.* **132**, 154104 (2010).
52. Henkelman, G., Uberuaga, B. P. & Jónsson, H. A climbing image nudged elastic band method for finding saddle points and minimum energy paths. *J. Chem. Phys.* **113**, 9901–9904 (2000).
53. Zhang, H., Qiu, L. & Hu, D. Finite-Temperature Dimer Method for Finding Saddle Points on Free Energy Surfaces. *J. Comput. Chem.* **40**, 1701–1706 (2019).
54. Abraham, M. J. *et al.* GROMACS: High performance molecular simulations through multi-level parallelism from laptops to supercomputers. *SoftwareX* **1–2**, 19–25 (2015).
55. Kaminski, G. A., Friesner, R. A., Tirado-Rives, J. & Jorgensen, W. L. Evaluation and Reparametrization of the OPLS-AA Force Field for Proteins via Comparison with Accurate Quantum Chemical Calculations on Peptides. *J. Phys. Chem. B* **105**, 6474–6487 (2001).
56. Sambasivarao, S. V. & Acevedo, O. Development of OPLS-AA Force Field Parameters for 68 Unique Ionic Liquids. *J. Chem. Theory Comput.* **5**, 1038–1050 (2009).

Figures

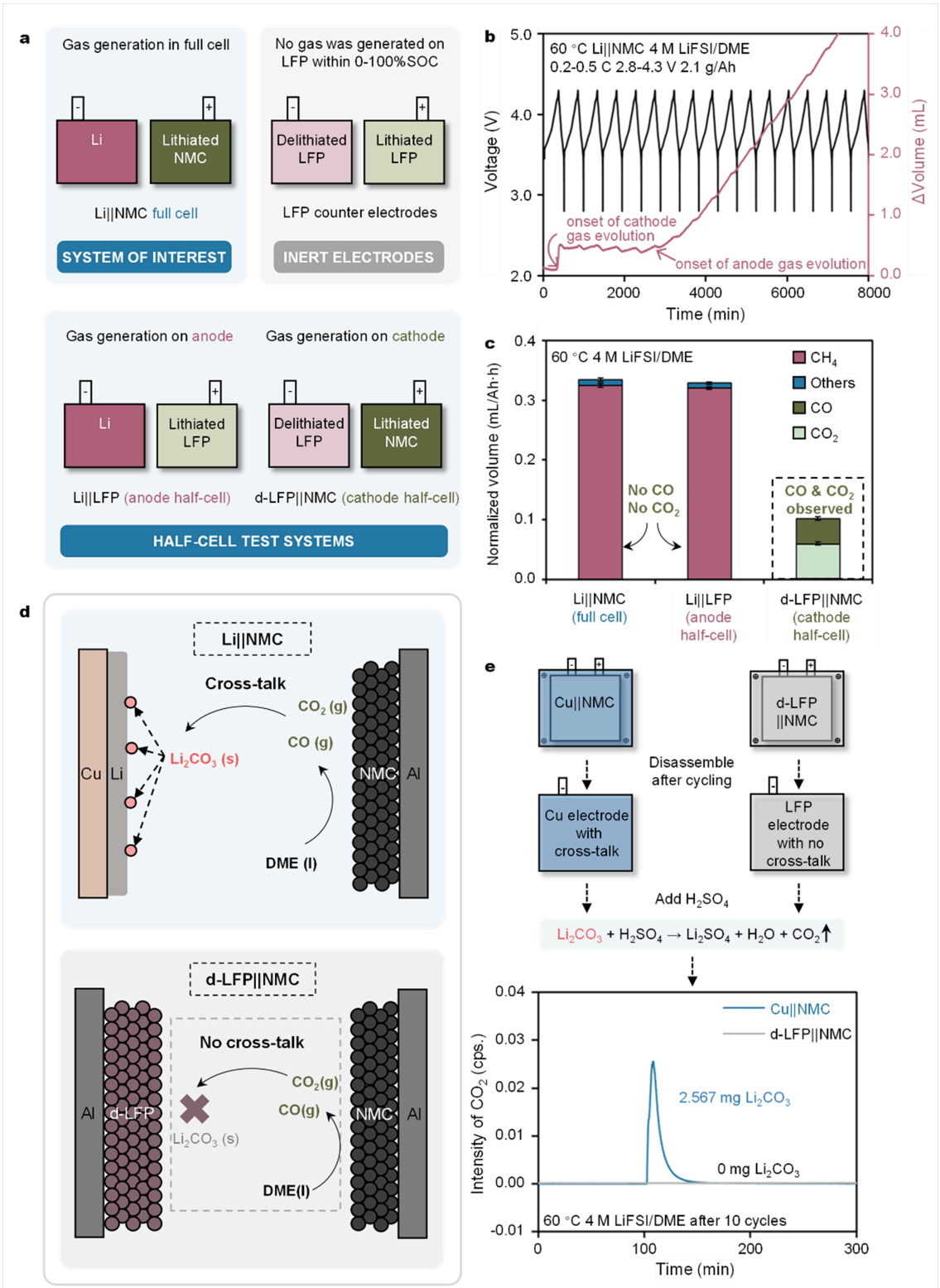

Figure 1

Investigating and quantifying gas evolution in LMB. a, Schematic of Li||NMC full cell, LFP counter electrodes, Li||LFP anode half-cell, and d-LFP||NMC cathode half-cell systems used to study gas evolution. **b**, Voltage (black) and change in cell volume (magenta) over time for a Li||NMC full cell with 4 M LiFSI/DME electrolyte cycled at 60 °C. **c**, Normalized volumes of gas components generated in Li||NMC, Li||LFP, and d-LFP||NMC cells. **d**, Schematic showing the presence or absence of cross-talk

phenomenon occurring in cells where CO and CO_2 are produced at the NMC surface. **e,** Schematic and CO_2 signal over time for the titration-mass spectroscopy experiment used to test for the presence of and to quantify the amount of one cross-talk product, Li_2CO_3.

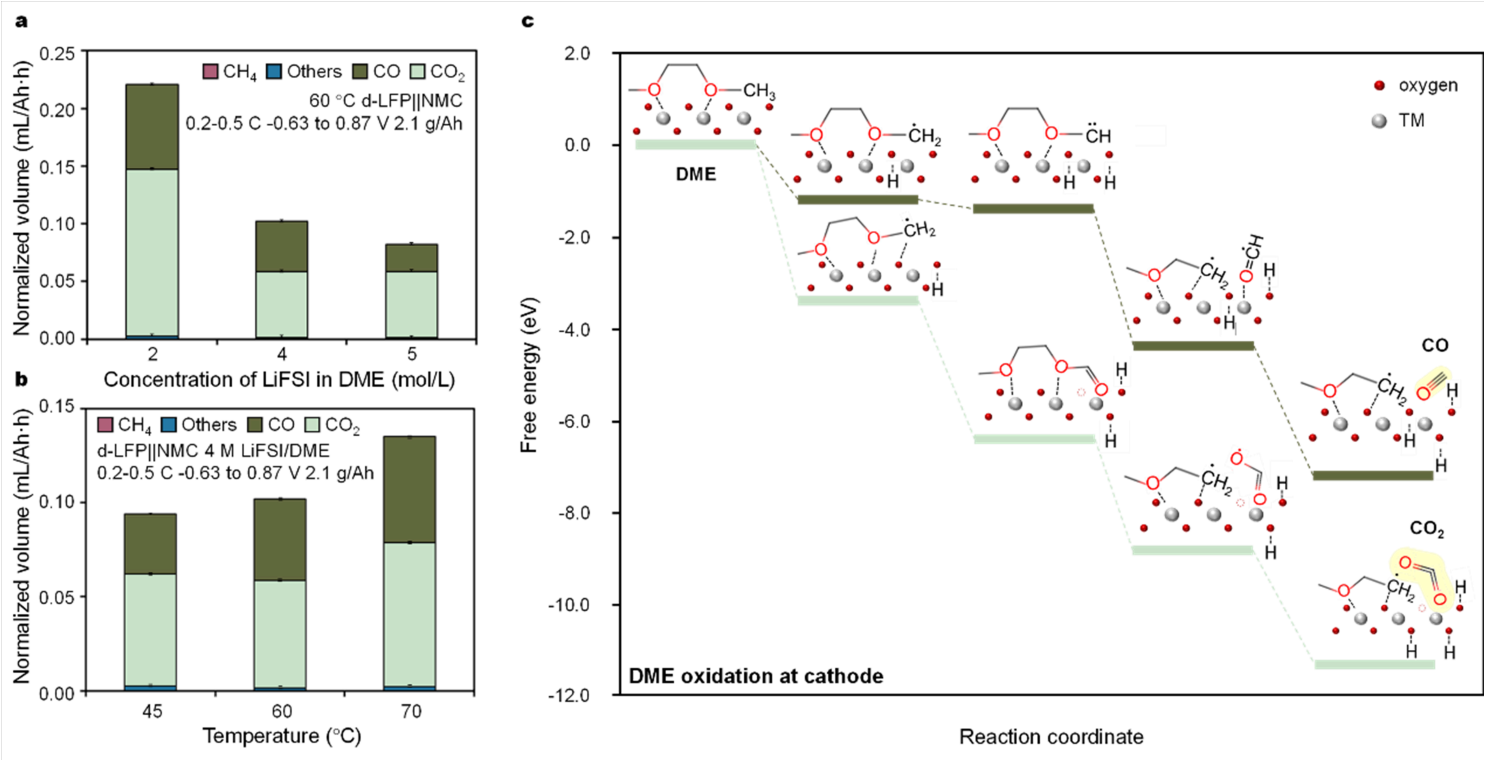

Figure 2

Gas evolution in a d-LFP||NMC cathode half-cell. Normalized gas volumes and gas component distributions **a,** at different concentrations (2, 4, 5 M) of LiFSI and **b,** at different temperatures (45, 60, 70 °C). **c,** Simulated pathways for the oxidation of DME into CO and CO_2.

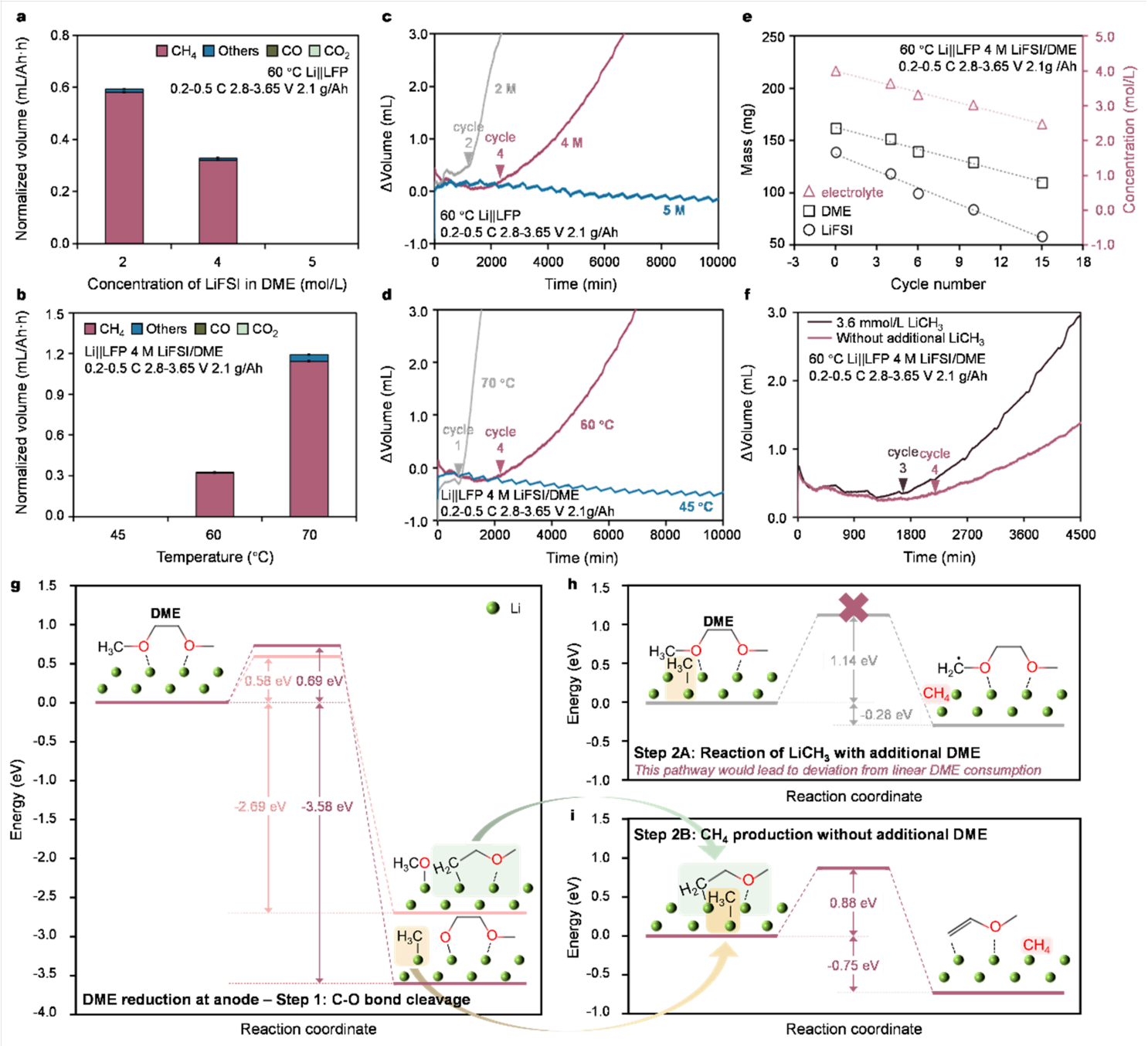

Figure 3

Gas evolution in a Li||LFP anode half-cell. (a, b) Gas volumes and gas component distributions **a,** at different concentrations (2, 4, 5 M) of LiFSI and **b,** at different temperatures (45, 60, 70 °C). **(c, d)** Corresponding changes in cell volume **c,** at different concentrations (2, 4, 5 M) of LiFSI and **d,** at different temperatures (45, 60, 70 °C). **e,** Electrolyte consumption results showing the decrease in the masses of DME (black squares) and LiFSI (black circles), as well as the overall decrease in the LiFSI/DME concentration (magenta triangles) over number of cycles. **f,** Change in cell volume over time for a Li||LFP cell with 4 M LiFSI/DME electrolyte cycled at 60 °C with and without added $LiCH_3$. **(g-i)** Simulated pathways for the formation of CH_4 at the anode. **g**, Step 1 involves C-O bond cleavages that result in two key intermediates (highlighted in green and light orange). There are two possible subsequent pathways:

h, Step 2A, in which $LiCH_3$ reacts with another DME to produce CH_4, and **i,** Step 2B, in which the two intermediates from Step 1 react to produce CH_4.

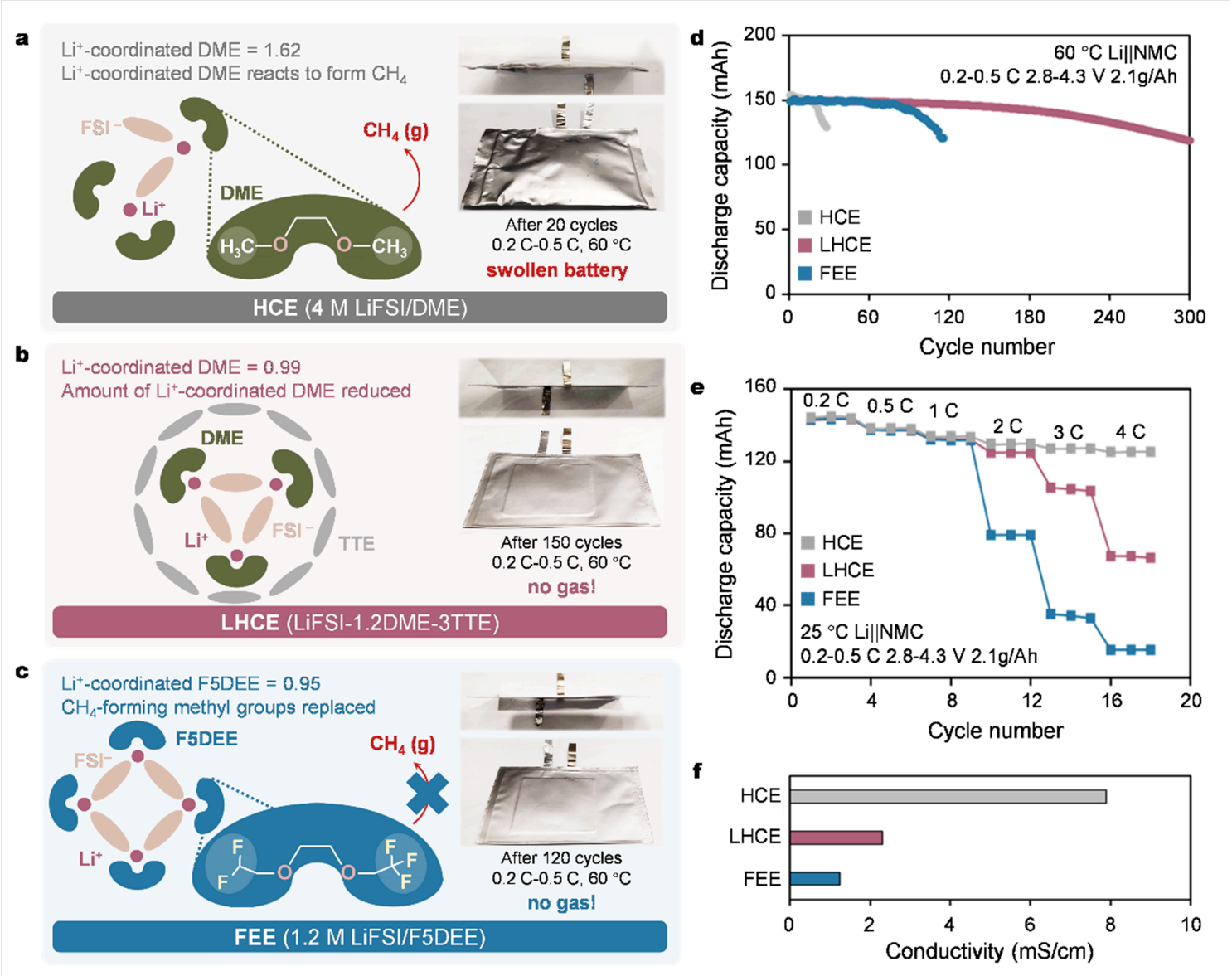

Figure 4

Schematic and properties of different electrolyte systems. a, For the HCE (4 M LiFSI/DME) system, there are, on average, 1.62 DME molecules coordinated to a Li^+ ion, and these DME molecules react to form CH_4, resulting in significant gas evolution, as observed in a Li||NMC cell after 20 cycles at 60 °C. **b,** For the LHCE (LiFSI-1.2DME-3TTE) system, there are, on average, 0.99 DME molecules coordinated to a Li^+ ion. The change in the solvation structure results in significantly reduced CH_4 production, and hence no gas evolution was observed after 150 cycles at 60 °C. **c,** For the FEE (1.2 M LiFSI/F5DEE) system, since the F5DEE molecules do not contain methyl groups, they do not react to form CH_4; no gas evolution was observed after 120 cycles at 60 °C. **d,** Cycling performance at 60 °C. **e,** Rate performance at 25 °C. **f,** Ionic conductivity values at 25 °C.

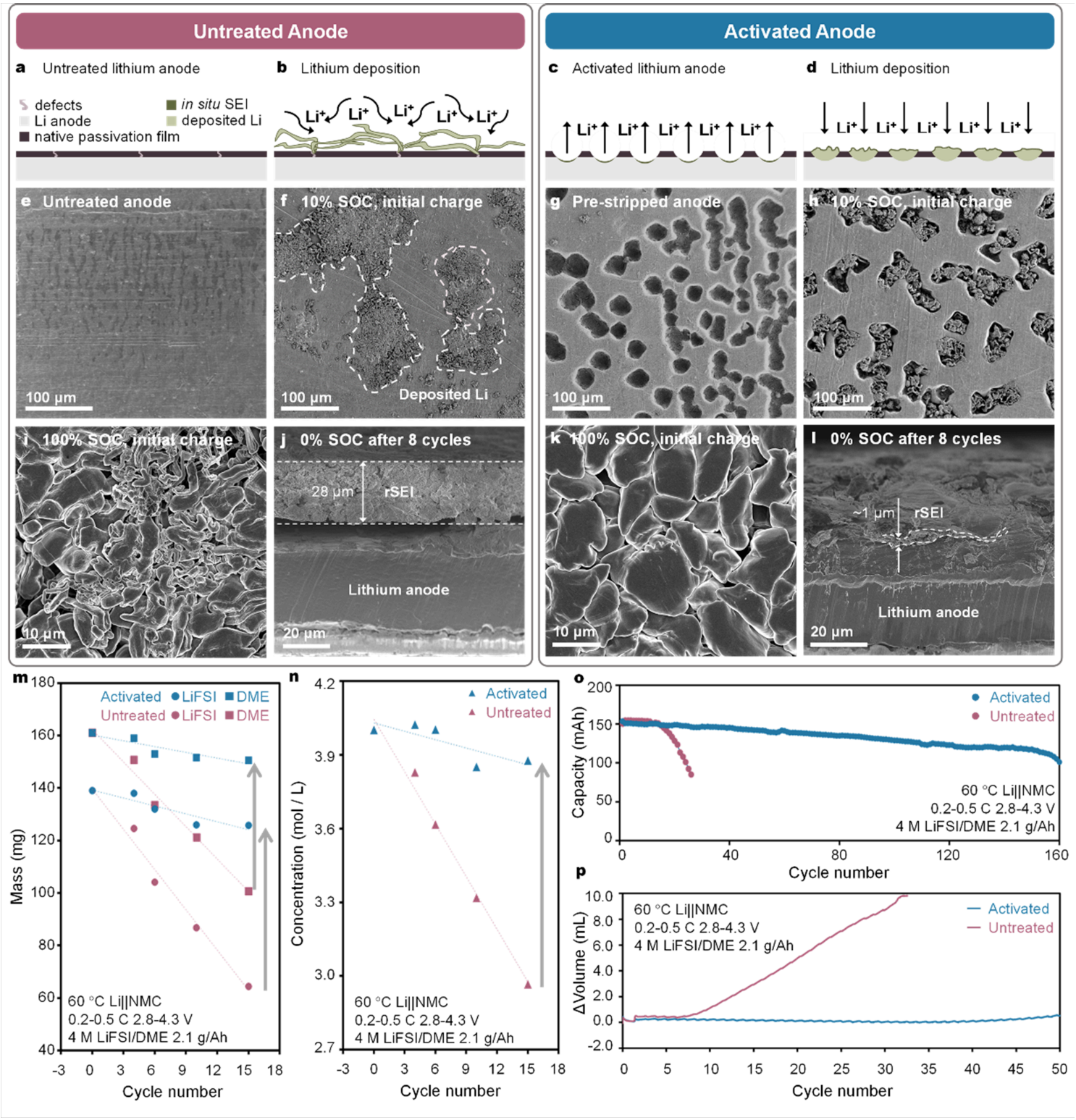

Figure 5

Li deposition morphology and performance of untreated and activated Li anodes. (a-d) Schematic showing Li deposition on untreated and activated Li anode surfaces. **a,** Untreated Li is covered by a native passivation film. **b,** Li dendrites grow from defect sites on the passivated surface. **c,** Activation of the Li anode by pre-stripping the surface to expose fresh Li, forming many pits. **d,** Li deposits within these pits in a more controlled manner. **(e-l)** SEM micrographs of untreated and activated Li anode

surfaces at various SOC. **e,** Untreated Li anode. **f,** Untreated anode with Li deposited at defect sites after an initial charge to 10% SOC. **g,** Pre-stripped (activated) anode with pits. **h,** Activated anode with Li deposited in the pits after an initial charge to 10% SOC. **i,** Untreated anode with Li dendrites covering the surface after an initial charge to 100% SOC. **j,** Cross-section of the untreated anode at 0% SOC after 8 cycles. The top layer is the rSEI. **k,** Activated anode with Li particles covering the surface after an initial charge to 100% SOC. **l,** Cross-section of the activated anode at 0% SOC after 8 cycles. The thin, top layer is the rSEI. **m,** Consumption of LiFSI (circles) and DME (squares) and **n,** decrease in LiFSI/DME concentration in Li||NMC cells at 60 °C with activated (blue) and untreated (magenta) Li anodes and corresponding **o,** cycling performance and **p,** changes in cell volumes.

Supplementary Files

This is a list of supplementary files associated with this preprint. Click to download.

- Supplementaryinformation.docx